Modelling of curtain effect in rockfall barrier with the dynamic relaxation

Romain Boulaud, Cyril Douthe, Karam Sab

Version of Record: https://www.sciencedirect.com/science/article/pii/S0020768320300147
Manuscript_e68a6142120aa90bf5c36237ae9e3e05

Modelling of curtain effect in rockfall barrier with the dynamic relaxation

R. BOULAUD[a], C. DOUTHE[a], K. SAB[a]

[a] *Laboratoire Navier, Ecole des Ponts Paritech, IFSTTAR, CNRS, UMR 8205, 6 et 8 avenue Blaise Pascal, Champs-sur-marne, France*

Abstract

Flexible rockfall barriers are protection systems against risks of falling rocks. Their complex behaviour is still not well understood and the development of relevant models allowing for quick calculations is a need toward the optimisation of such structures. The key issue is the modelling of the so-called "curtain effect", where the cable net slides along the supporting cables. The present paper proposes hence a model of sliding cable submitted to concentrated forces. It addresses the stability conditions of the centred finite difference scheme, especially in the framework of the Dynamic Relaxation Method where estimates are found for the best possible fictitious masses at nodes. Expressions are derived in the general case, but also for monotonically curved cables and looped cable elements or rings. Elementary problems are shown for validation, before a case study based on experiments conducted during the French National project C2ROP demonstrates the accuracy and the reliability of the proposed methodology. The present study is however limited to quasi-static loadings and therefore needs further developments to be extended to realistic dynamic cases which are discussed in the conclusion.

Keywords: Discrete element method, numerical stability, sliding cable, dynamic relaxation, ring element, anti-submarine net.

1. Introduction

1.1. General context

The hazard of landslide, mainly in mountain areas, compromises the safety of inhabitants. The need to protect them, their properties and infrastructures against this risk requires the setting of protective structures. Rockfall barrier is an often used alternative because of its low weight and its high capacity to absorb energy. It can be installed, by specialised workers, on hard-to-reach areas. These structures are complex and involve non-standard connections in civil engineering. Schematically, their behaviour can be described as follows: a wire net (shown in Figure 1, but not necessarily) intercepts the rock trajectory. It then deforms, sliding along the supporting cables which are attached to the posts or the cliff by dissipating devices that undergo irreversible transformations by yielding, rubbing or tearing. The dissipation of the rock kinetic energy is thus insured by the friction and plastic deformation of the net itself and by the brakes distributed along the cables. The sliding of the rings along each other and along the supporting cables is essential to the behaviour of the barrier: it allows the members to be rearranged in such a way that the structure can withstand the impact without stress concentration and adapt to any location of the impact. The proper modelling of the sliding should give more insight into a very non-linear problem, and help to improve the results of companies trying to get an agreement for their products. It was indeed shown in [8] that one out of two tests at the French experimental testing facility in Montagnole was negative.

Figure 1: Top view of the rockfall barrier prototype developed in the framework of the french national project C2ROP (Photo courtesy of NP C2ROP).

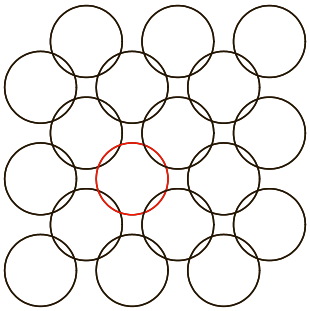

Figure 2: Pattern of a ASM4 ring net.

Indeed, 2008, a European Technical Agreement (ETA) was set for flexible rockfall barriers in order to align the design standards between the EU countries. This agreement is in line with the recommendations of the technical guide ETAG 027, which is the reference publication for the design of barriers [15]. To receive it, the structure must withstand the fall of a block with a given energy with controlled deformation. The full-scale test procedure, proposed by the ETAG 027, is largely driven by the previous experiments on complete structures carried out by manufacturers and academics. We can notably mention the experiments of D. Peila (1998), where the block is guided by a trolley before the impact on the net [25] and the experiments of H. Grassl (2002) in partnership with the Swiss company Geobrugg [18]. A product is hence approved for one critical energy level. Despite the development of powerful computational tools in the last decades [19, 28, 7, 18], this experiment is today the only recognised way to validate the performance of a flexible barrier.

1.2. The Dynamic Relaxation Method

The behaviour of the flexible barriers reveals strong geometric and material non-linearities, so that their modelling is complex and their calculations are time consuming, especially when the full dynamic simulation is conducted. The development of a modelling strategy that would allow quick calculations and parametric studies would thus be of great help in the comprehension of their complex behaviour and toward the development of new barriers. The key issue is the modelling of sliding cables which is addressed here, with a focus on a stability condition with the Dynamic Relaxation Method (DRM). The dynamic relaxation method is a discrete numerical method used to determine the equilibrium state of a system

submitted to mechanical loads which is very suitable for large displacement [13]. Its principle consists in linearising the differential equation of the Newton's first law by an explicit scheme of numerical integration. The static position of a structure is hence considered as the result of a smoothed dynamical process.

If the forces are conservative, the dynamical behaviour of the system has no influence on its equilibrium state. The dynamic parameters (damping and mass) can thus be chosen to optimise the convergence of the algorithm. M. Papadrakakis proposed a general method to identify the critical parameters of a structure [24], but it is relatively complex and does not significantly outperform other methods [27]. That's why an alternative artificial damping, the "kinetic damping" proposed by P. Cundall, is used in the algorithm presented in this paper [12]. It is based on the principle of mechanical energy conservation during an undamped dynamic process. Considering that in this case, each minimum of potential energy coincides with a maximum of kinetic energy, setting artificially the kinetic energy to zero at every peak should lead progressively to the equilibrium state. This method is very popular among others [5, 6, 14], so that in the rest of this paper, numerical simulations will be carried out with a DR algorithm using kinetic damping.

This quasi-static modelling rely on the idea that the block will concentrate most of the inertial forces and of the kinetic energy, as the mass of the block is generally five times greater than the mass of the net and that initially only the block is moving. It also relies on the fact that the brakes serve as fuses for the anchorages and surrounding cables or supporting members, cutting off peaks that may occur in usual impact problems. Therefore, a quasi-static calculation of the equilibrium state should give a quick and reasonable estimate of

the equilibrium configuration after impact and hence provides to the engineer some useful global information of the barrier, such as estimates of the residual height, the brakes stroke or the depth of the net. The loading equivalence between static and dynamic loadings would then be based on the dissipated energy, not on forces. These assumptions build on preliminary results of the C2ROP research project [23] where similar quasi-static and dynamic experiments were conducted and evidenced similarity in the barrier behaviour (see the load-displacement curves of figure 3, note that for the dynamic test the load is calculated from the product mass time measured acceleration of the block.)

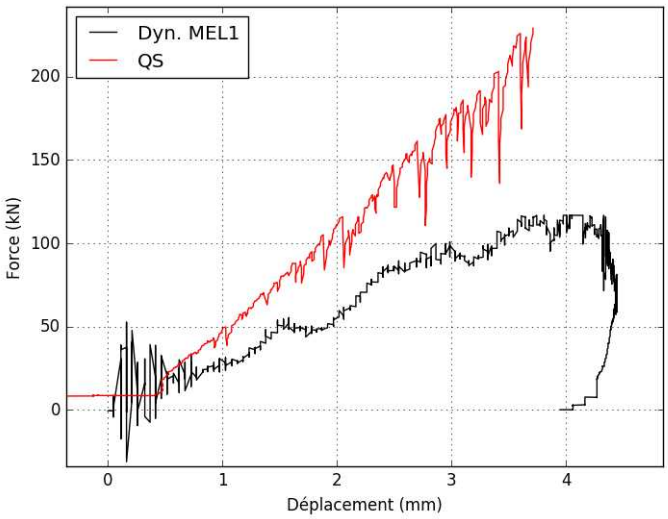

Figure 3: Comparison of quasi-static /dynamic experimental global behaviour of the C2ROP fence (by courtesy PN C2ROP).

However the net itself is not protected by the brakes and their fuses role. Therefore it needs to be underligned here that the dynamic aspects of the impact can not be predicted by the proposed quasi-static analysis which would fail to estimate maximum forces in the

net due to back lash as well as local stress concentration around the block, which is known as "bullet effect" and tightly linked with the form and speed of the block (see for instance [19]).

1.3. "Curtain effect" and sliding cable

As just said in the previous section, the modelling of the "curtain effect" is key to the understanding of the structure behaviour: when a block impacts the interception structure, the net slides along the support cables and tends to concentrate around the impacted zone. The geometric reorganisation, created by the sliding of the net, allows to increase the motion (in the vertical direction) of the complete structure, hence minimising the internal forces. This phenomenon, illustrated in Figure 4, is called "curtain effect" and is commonly modelled with a "sliding cable" [18], whose tension depends on the variation of its whole length. ~~The tension is hence constant in the cable and does not depend on the relative positions of successive nodes.~~

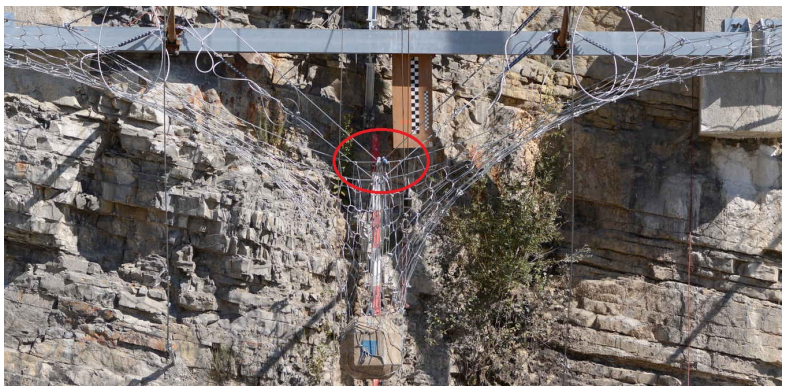

Figure 4: "Curtain effect" due to block impact (by courtesy PN C2ROP).

We can find a few models of such elements in the literature. The list of works presented

here is not exhaustive. B. Zhou developed in 2004 a 3-nodes sliding cable model for an application to parachute systems [29]. A generalisation is proposed by C. Chen for a digital implementation in a FEM software in the purpose of studying the resistance of a dome [9]. L. Ghoussoub [17] also proposed a generalisation of the sliding model of B. Zhou to n-nodes cable [29].

An alternative approach of the sliding of the cable through the post head was also proposed using dedicated Master and Slave nodes by Gentilini *et al* [16] and Tran *et al* [26], while Albaba *et al* proposed a rigid closed loop connections, formed by four nodes, and through which the cable passes [1].

Another part of its field of use is also the case of cables passing through pulleys. This system is widely used in the industry to transfer loads on long and complex path. The particularity of pulleys is that they can apply a friction force on the cable so that tension is different on each side of it. M. Aufaure proposed a first finite element model of a cable passing through one pulley to describe the deformation of a power line [2, 3]. This work was then extended by F. Ju to identify the tangent stiffness matrix of a cable passing through n pulleys. While staying in the framework of pulleys system, K. Hincz conducted a nonlinear analysis with the DR method to determine the geometry of an arch-supported cable net roof [20] and A. Bel Hadj *et al* proposed a model taking into account a friction force [5, 6]. J. Coulibaly used also this approach to propose a model adapted to rockfall barriers and included friction forces [10]. In Coulibaly *et al* [10] as well as in Bel Hadj *et al* [6], the parametric studies show that friction might have a significant influence on the static equilibrium and dynamic of lightweight structures.

However, in the specific case studied here, the experiments on the rockfall barriers conducted in [23] have shown that the sliding occurs at the very beginning of the impact, so that it occurs on a configuration with low angles between cable successive elements (θ) and with low forces in cables (T). Therefore one might estimate that the friction evaluated from the friction coefficient μ as $T(exp(\mu\theta) - 1)$ is low and that the associated dissipated energy is negligible compared to the energy dissipated by the brakes. Also the fact that the sliding cables are always linked with brakes at each end ensures that the magnitude of the tension in the cable end is fixed by the brakes threshold which is quickly reached during the impact and almost independently of the friction coefficient. A frictionless sliding cable should thus be able to capture the behaviour of the barrier at leading order.

1.4. Summary of contributions

The next two sections are hence dedicated to the discrete modelling of frictionless sliding cables and its numerical stability within the framework of a dynamic explicit scheme, with application to n-nodes monotonic supporting cables and ring nets. Some computations are carried in the fourth section on simple examples to assess the accuracy and stability of the numerical models. Finally, a case-study on a quasi-static experiment on a whole barrier prototype is proposed and demonstrates the interest of the frictionless proposed model. Some perspectives on the limitation of the present study and possible extensions will conclude the paper.

2. Modelling of a sliding cable element

As presented in introduction the "curtain effect" is currently modelled by means of a sliding cable element. Cables are connected to the rings along each edge of the net. In view of the diameters of cables and rings, a single contact point can be considered between these two elements. Such cables can either be modelled as continuous elements submitted to concentrated forces, or discretely as an ordered set of nodes linked together by spring interactions. The main purpose of this section is to identify the tangent stiffness matrix of a frictionless sliding cable, which is necessary to determine a stability condition of the centred finite difference scheme [24]. In a first subsection, the expression of the internal forces vector will first be identified as a function of displacements from the equilibrium of a continuous cable submitted to n concentrated forces. This straightforward approach is well-known and will allow us to correctly introduce the notations required to define the discrete internal forces vector. Moreover, it will be demonstrated that, with this case of concentrated forces, results do not depend on the description of the problem (continuous or discrete). The second subsection will be dedicated to the identification of the tangent stiffness matrix of a sliding cable. From its expression, a stability condition of the finite differences scheme will be proposed in a third section, easily calculable, in order to reduce computation costs.

2.1. Equilibrium of a sliding cable submitted to concentrated forces

2.1.1. Definition

We propose to write the equilibrium of a cable loaded by n concentrated forces (which may represent n rings connected to the cable in a rockfall barrier). A cable of length l

is represented as a uni-dimensional element and parametrised by its arc-length, so that $\forall\, s \in [0; l]$, the position of a point s along the cable is given by: $s \to \underline{x}(s)$. We also consider the n forces $\underline{f}_i$ applied on the points of curvilinear abscissa: $s_1 < ... < s_n$ with $s_1 = 0$ and $s_n = l$.

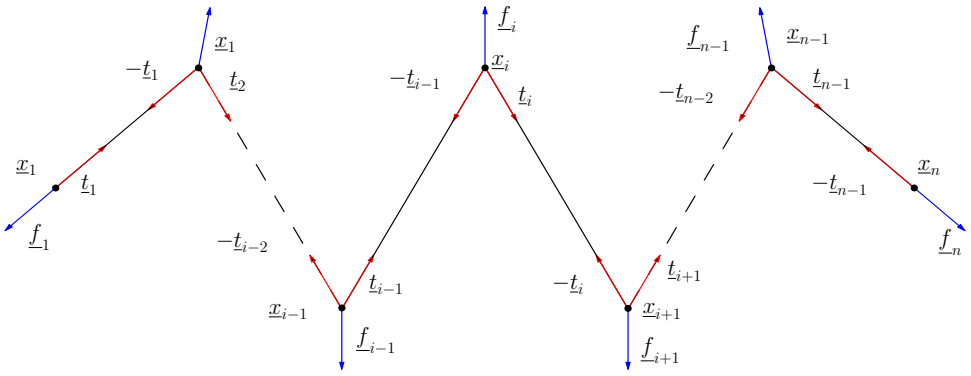

Figure 5: Equilibrium of a sliding cable under concentrated forces (assuming $\underline{t}_i = -\underline{t}(s_{i+1}^-) = \underline{t}(s_i^+)$)

.

In the rest of this section, the following assumptions will be considered:

- The function $s \to \underline{x}(s)$ is piece-wise differentiable. The tangent vector is hence defined on each interval where f is differentiable by: $\underline{t} : s \to \frac{d\underline{x}(s)}{ds}$.
- Since the bending and compression stiffness are considered as null, the cable can only undergo tensile forces.
- The tensile force is uniform along the cable and given by: $\underline{T}(s) = T\underline{t}(s)$ with $s \in]0, l[$ when t is defined.

- Considering the large displacements of the cable, all the equilibrium equations are established on the deformed geometry.

Let $ds_i \in \left]0, \min\left(\frac{1}{2}||\underline{x}(s_i) - \underline{x}(s_{i-1})||\,,\, \frac{1}{2}||\underline{x}(s_{i+1}) - \underline{x}(s_i)||\right)\right[$. Firstly, we write the equilibrium of a cable segment between two consecutive forces. The segment $[s_i + ds_i, s_{i+1} - ds_i]$ is not loaded by any external force and its equilibrium is simply given by:

$$T\underline{t}(s_i + ds_i) = T\underline{t}(s_{i+1} - ds_i) \tag{1}$$

The cable is thus necessarily straight between two concentrated forces and

$$\underline{t}(s_i^+) = \underline{t}(s_{i+1}^-) = \frac{\underline{x}(s_{i+1}) - \underline{x}(s_i)}{||\underline{x}(s_{i+1}) - \underline{x}(s_i)||} \tag{2}$$

Then, the equilibrium of any segment $[s_i - ds_i, s_i + ds_i]$ on which the force $\underline{f}_i$ is applied gives the change of tangent direction at the node:

$$T\left(\underline{t}(s_i^+) - \underline{t}(s_i^-)\right) = \underline{f}_i \tag{3}$$

Finally, to describe the equilibrium of the whole cable, it still remains to write the equilibrium of its two extremities:

$$-T\underline{t}(s_1^+) = \underline{f}_1 \quad \text{and} \quad T\underline{t}(s_n^-) = \underline{f}_n \tag{4}$$

The deformed geometry of the cable is hence piece-wise linear and it is completely given by the position of the points on which the forces are applied (see Figure 5). The equilibrium

of the whole cable $\underline{F}^{int} = \underline{F}^{ext}$ writes hence:

$$T \begin{bmatrix} \underline{t}(s_1^+) \\ \vdots \\ \underline{t}(s_i^+) - \underline{t}(s_i^-) \\ \vdots \\ -\underline{t}(s_n^-) \end{bmatrix} + \begin{bmatrix} \underline{f}_1 \\ \vdots \\ \underline{f}_i \\ \vdots \\ \underline{f}_n \end{bmatrix} = 0 \tag{5}$$

The transition from the equilibrium of a continuous cable under multiple concentrated forces to the discrete model is thus obvious. The discrete model is completely determined by the ordered set of the n nodes positions $[\underline{x}(s_1) \dots \underline{x}(s_i) \dots \underline{x}(s_n)]$ of the continuous cable which now will be simply noted $[\underline{x}_1 \dots \underline{x}_i \dots \underline{x}_n]$ for a discrete cable. The tangent vectors can always be defined in the same way but for the sake of clarity, only the right side tangent will be considered:

$$\underline{t}_i = \frac{\underline{\Delta x}_i}{l_i} \quad \text{with} \quad \underline{\Delta x}_i = \underline{x}_{i+1} - \underline{x}_i \quad \text{and} \quad l_i = ||\underline{x}_{i+1} - \underline{x}_i|| \tag{6}$$

The components of the vector $\underline{t}_i$ in the direct orthogonal system $(\underline{e}_1, \underline{e}_2, \underline{e}_3)$ are respectively noted: $t_{1,i}, t_{2,i}, t_{3,i}$.

We assume then that the behaviour of the element is linear elastic and characterised by Hooke's law. Noting respectively E , S and ϵ, the Young's modulus, the cross section and the uniform strain of the cable, the tensile force is simply given by:

$$T = ES\epsilon \tag{7}$$

where ϵ can be evaluated from the deformed length of each segment and the global rest

length l_0 :

$$\epsilon = \frac{1}{2}\left(\left(\frac{\sum_{i=1}^{n-1} l_i}{l_0}\right)^2 - 1\right) \quad \text{with} \quad l_0 = \sum_{i=1}^{n-1} l_i^{rest} \tag{8}$$

Considering the previous notations, the expression of the internal forces vector (5) in frictionless cables can be rewritten on the nodal displacements basis:

$$\underline{F}^{int} = ES\epsilon \begin{bmatrix} -t_{1,1} \\ \vdots \\ t_{1,i-1} - t_{1,i} \\ t_{2,i-1} - t_{2,i} \\ t_{3,i-1} - t_{3,i} \\ \vdots \\ t_{3,n-1} \end{bmatrix} \tag{9}$$

2.1.2. Remarks

Before proceeding with the determination of the tangent stiffness matrix, it is interesting to discuss the form of the internal forces vector (9).

Eulerian vs Lagrangian. As explained in the introductory paragraph of this section, similar studies to identify the tangent stiffness matrix of a sliding cable have been already carried out. B. Zhou [29], C. Chen [9] and L. Ghoussoub [17] have established an expression of the tangent stiffness matrix for a 3 or n nodes sliding cable respectively; the developments of C. Chen and L. Ghoussoub being a generalisation of the problem dealt by B. Zhou. Through their demonstration, they naturally identify an internal forces vector F_{ante}^{int} which

can be compare to the present internal force vector $F^{int}_{present}$, such that:

$$F^{int}_{present} = \left(l_{final}/l_{initial}\right)^2 F^{int}_{ante} \tag{10}$$

The expressions of the internal forces vector (9) developed in the present paper thus differ from the one defined by C. Chen and L. Ghoussoub by the square of the lengths ratio. The study of the three demonstrations indicates that, while writing the virtual work of the element, a confusion between the Eulerian and the Lagrangian strains had been made, as well as in the choice of the reference configuration for the Cauchy stress tensor, with the consequence for the whole scheme not to be consistent. Indeed the Cauchy stress tensor σ lies in the deformed (Eulerian) configuration while the deformation considered by previous authors corresponds to the Lagrangian deformation tensor ϵ which is built on the initial configuration. The strain energy considered is thus an hybrid product of one Eulerian object and one Lagrangian object which is not consistent. To be correct, it requires to take into account the metric changes between Eulerian and Lagrangian deformation $\left(\frac{ds'}{ds}\right)^2 = \left(l_{initial}/l_{final}\right)^2$ which would cancel the additionnal term in (10). It is thus claimed that the actual formulation is the correct one. Moreover the consistency of the present model is highlighted by the fact that, in the case of concentrated forces, the discrete model becomes fully equivalent to the continuous description.

Discrete normal vectors. The main assumption of a sliding cable model involves that, the external forces are orthogonal to the cable tangent in the deformed geometry. The demonstration is relatively simple in the case of distributed forces and was done above for concentrated forces. The cable being not continuously differentiable, it is impossible to define the

normal vector to the curve wherever a concentrated force is applied, but a discrete normal vector can be defined. Actually one of the usual approaches is to set it as the direction given by the bisector of two successive tangents (see Figure 5):

$$\underline{n}_i = \frac{\underline{t}_{i+1} - \underline{t}_i}{||\underline{t}_{i+1} - \underline{t}_i||} \tag{11}$$

The norm of $\underline{t}_{i+1} - \underline{t}_i$ depends on the discrete turning angle θ, which is the angle between $\underline{t}_{i+1}$ and $\underline{t}_i$:

$$||\underline{t}_{i+1} - \underline{t}_i|| = 2|\sin\frac{\theta}{2}| \tag{12}$$

Comparing (11) with (9), we notice that the intensity of the internal forces depends on the local discrete normals of the cable. Therefore, in order to simplify notations in the rest of this section, even if the internal forces at the points x_1 and x_n are not directed by the discrete normal (which can not be defined at these points), we will note $\underline{N}$ the vector such that: $\underline{F}^{int} = ES\epsilon\underline{N}$ in (9), so that $\underline{N}$ is defined by:

$$\underline{N}^T = [-t_{1,1}, \ldots, t_{1,i} - t_{1,i-1}, t_{2,i} - t_{2,i-1}, t_{3,i} - t_{3,i-1}, \ldots, t_{3,n-1}] \tag{13}$$

2.2. Identification of the tangent stiffness matrix

The expression of internal forces in a sliding cable as a function of its nodal displacements have been identified in the previous section. It should be noted that the description of the cable equilibrium was only a way of achieving this result and the expression can be extended to any kinematically admissible displacement. This section is dedicated to the identification of the sliding cable tangent stiffness matrix. It is currently calculated from the expression of the internal forces vector (9) by:

$$\underline{\underline{K}} = grad_{\underline{U}}(\underline{F}^{int}) \tag{14}$$

where $\underline{U}$ is the vector of the actual or eulerian nodal displacements. $\underline{F}^{int}$ and $\underline{U}$ are vectors of size $3n$ and, to avoid any confusion, their components will be indexed with the index $j \in [1, 3n]$, whereas the nodes of the discrete cable are indexed with the index $i \in [1, n]$. For example, considering that $j = 3i$ and using the expression (9) it will be noted:

$$F_j^{int} = ES\epsilon N_j = ES\epsilon\left(t_{1,i-1} - t_{1,i}\right) , \quad F_{j-1}^{int} = ES\epsilon\left(t_{3,i-2} - t_{3,i-1}\right) , \quad F_{j+1}^{int} = ES\epsilon\left(t_{2,i-1} - t_{2,i}\right) \tag{15}$$

The same notations are considered for the nodal displacements, and the components of the matrix $\underline{\underline{K}}$ can now be expressed:

$$K_{jk} = \frac{\partial F_j^{int}}{\partial U_k} = ES\left[N_j \frac{\partial \epsilon}{\partial U_k} + \epsilon \frac{\partial N_j}{\partial U_k}\right] \tag{16}$$

In order to simplify the rest of the development, $\underline{\underline{K}}$ is considered as the sum of two square matrices: the elastic stiffness matrix and the geometric stiffness matrix, respectively noted $\underline{\underline{K}}_E$ and $\underline{\underline{K}}_G$:

$$K_{E,jk} = ESN_j \frac{\partial \epsilon}{\partial U_k} , \quad \text{and} \quad K_{G,jk} = ES\epsilon \frac{\partial N_j}{\partial U_k} \tag{17}$$

It remains now to calculate the two partial derivatives. Firstly, we determine the expression of $\underline{\underline{K}}_E$. The uniform strain of the cable is given by (8), which depends on the deformed length of each segment. According to the notations introduced in (6), it can be expressed as:

$$l_i = \sqrt{\Delta x_{1,i}^2 + \Delta x_{2,i}^2 + \Delta x_{3,i}^2} \tag{18}$$

We can hence write:

$$\frac{\partial \epsilon}{\partial U_k} = \frac{l}{l_0^2} \sum_{i=1}^{n-1} \left[\frac{1}{2l_i}\left(\frac{\partial \Delta x_{1,i}^2}{\partial U_k} + \frac{\partial \Delta x_{2,i}^2}{\partial U_k} + \frac{\partial \Delta x_{3,i}^2}{\partial U_k}\right)\right] \tag{19}$$

Now we use the nodal displacement indexing and Kronecker symbol δ_{jk} to develop this expression:

$$\frac{\partial \epsilon}{\partial U_k} = \frac{l}{l_0^2} \sum_{j=1}^{3n-3} \left[\frac{x_{j+3} - x_j}{l_j} \left(\frac{\partial x_{j+3}}{\partial U_k} - \frac{\partial x_j}{\partial U_k} \right) \right] = \frac{l}{l_0^2} \sum_{j=1}^{3n-3} \left[\frac{x_{j+3} - x_j}{l_j} \left(\delta_{(j+3)k} - \delta_{jk} \right) \right] \tag{20}$$

Finally, the coefficients of the $\underline{\underline{K}}_E$ matrix are defined as follows:

$$K_{E,jk} = \frac{ES}{l_0} N_j \begin{cases} -\frac{l}{l_0} \frac{x_{k+3} - x_k}{l_k} & \text{if} \quad k \in [1,3] \\ \frac{l}{l_0} \left(\frac{x_k - x_{k-3}}{l_{k-3}} - \frac{x_{k+3} - x_k}{l_k} \right) & \text{if} \quad k \in [4, 3n-3] \\ \frac{l}{l_0} \frac{x_k - x_{k-3}}{l_{k-3}} & \text{if} \quad k \in [3n-2, 3n] \end{cases} \tag{21}$$

The expression of the discrete normal $\underline{N}$ is recognised in the expression after the bracket, so that:

$$\underline{\underline{K}}_E = \frac{ES}{l_0} \frac{l}{l_0} \underline{N} \otimes \underline{N} = K_0 \frac{l}{l_0} \underline{N} \otimes \underline{N} \tag{22}$$

The second part of the stiffness matrix $\underline{\underline{K}}_G$ depends on the coefficients $\frac{\partial N_j}{\partial U_k}$. The global indexing is still used and, to clarify the rest of the developments, we consider that j is a multiple of 3, even if there are no difficulties of computation in the other cases. We consider the general case where $j \in [4, 3n-3]$ and once again different sub-cases must be considered.

$$\frac{\partial N_j}{\partial U_k} = \frac{\partial}{\partial U_k} \left(\frac{x_j - x_{j-3}}{l_{j-3}} - \frac{x_{j+3} - x_j}{l_j} \right) \tag{23}$$

After developments,

$$\frac{\partial N_j}{\partial U_k} = \frac{\delta_{jk} l_{j-3} - \frac{\partial l_{j-3}}{\partial U_k} x_j}{l_{j-3}^2} - \frac{\delta_{(j-3)k} l_{j-3} - \frac{\partial l_{j-3}}{\partial U_k} x_{j-3}}{l_{j-3}^2} - \frac{\delta_{(j+3)k} l_j - \frac{\partial l_j}{\partial U_k} x_{j+3}}{l_j^2} + \frac{\delta_{jk} l_j - \frac{\partial l_j}{\partial U_k} x_j}{l_j^2} \tag{24}$$

Using (18), the coefficients are given by:

- $k = j$:

$$\frac{\partial N_j}{\partial U_j} = \frac{l_{j-3}^2 - (x_j - x_{j-3})^2}{l_{j-3}^3} + \frac{l_j^2 - (x_{j+3} - x_j)^2}{l_j^3} \tag{25}$$

- $k = j - 3$:

$$\frac{\partial N_j}{\partial U_{j-3}} = \frac{(x_j - x_{j-3})^2 - l_{j-3}^2}{l_{j-3}^3} \tag{26}$$

- $k = j + 3$:

$$\frac{\partial N_j}{\partial U_{j+3}} = \frac{(x_{j+3} - x_j)^2 - l_j^2}{l_j^3} \tag{27}$$

- $k = j - 2$:

$$\frac{\partial N_j}{\partial U_{j-2}} = \frac{(x_j - x_{j-3})(x_{j+1} - x_{j-2})}{l_{j-3}^3} \tag{28}$$

- $k = j - 1$:

$$\frac{\partial N_j}{\partial U_{j-1}} = \frac{(x_j - x_{j-3})(x_{j+2} - x_{j-1})}{l_{j-3}^3} \tag{29}$$

- $k = j + 1$:

$$\frac{\partial N_j}{\partial U_{j+1}} = -\frac{(x_j - x_{j-3})(x_{j+1} - x_{j-2})}{l_{j-3}^3} - \frac{(x_{j+3} - x_j)(x_{j+4} - x_{j+1})}{l_j^3} \tag{30}$$

- $k = j + 2$:

$$\frac{\partial N_j}{\partial U_{j+2}} = -\frac{(x_j - x_{j-3})(x_{j+2} - x_{j-1})}{l_{j-3}^3} - \frac{(x_{j+3} - x_j)(x_{j+5} - x_{j+2})}{l_j^3} \tag{31}$$

- $k = j + 4$:

$$\frac{\partial N_j}{\partial U_{j+4}} = \frac{(x_{j+3} - x_j)(x_{j+4} - x_{j+1})}{l_j^3} \tag{32}$$

- $k = j + 5$:

$$\frac{\partial N_j}{\partial U_{j+5}} = \frac{(x_{j+3} - x_j)(x_{j+5} - x_{j+2})}{l_j^3} \tag{33}$$

- $k \notin [j - 3, j + 5]$

$$\frac{\partial N_j}{\partial U_k} = 0 \tag{34}$$

The extension of previous calculations to the next two lines allows to construct the following 3×3 matrix, whose coefficients are written with the index i running from 1 to n.

$$\underline{\underline{A_i}} = -\frac{1}{l_i^3} \begin{pmatrix} \Delta x_{1,i}^2 - l_i^2 & \Delta x_{1,i}\Delta x_{2,i} & \Delta x_{1,i}\Delta x_{3,i} \\ & \Delta x_{2,i}^2 - l_i^2 & \Delta x_{2,i}\Delta x_{3,i} \\ sym & & \Delta x_{3,i}^2 - l_i^2 \end{pmatrix} \tag{35}$$

The matrix $\underline{\underline{K}}_G$ of size $3n \times 3n$ is thus sparse and writes in accordance with the sub-matrix $\underline{\underline{A}}_i$ as follows:

$$\underline{\underline{K}}_G = ES\epsilon \begin{pmatrix} \underline{\underline{A}}_1 & -\underline{\underline{A}}_1 & 0 & & & & \cdots & 0 \\ & \underline{\underline{A}}_1 + \underline{\underline{A}}_2 & -\underline{\underline{A}}_2 & 0 & & & \cdots & 0 \\ & & \ddots & \ddots & \ddots & & \cdots & \vdots \\ & & & \underline{\underline{A}}_{i-1} + \underline{\underline{A}}_i & -\underline{\underline{A_i}} & 0 & \cdots & 0 \\ & sym & & & \ddots & \ddots & \cdots & \vdots \\ & & & & & & \underline{\underline{A}}_{n-2} + \underline{\underline{A}}_{n-1} & -\underline{\underline{A}}_{n-1} \\ & & & & & & & \underline{\underline{A}}_{n-1} \end{pmatrix} \tag{36}$$

This finishes the determination of the tangent stiffness matrix of a n-nodes sliding cable.

2.3. Stability condition of the Dynamic relaxation scheme

2.3.1. Definition of a general condition

M. Papadrakakis proposed a general method to identify the critical parameters of a structure made of springs in the framework of the dynamic relaxation algorithm [24]. This method has been taken over by many authors, including M. Barnes who formulated a simple

expression insuring the stability of the algorithm with kinetic damping [4]:

$$m_i \geq \frac{\Delta t^2}{2} {K_i}^{max} \tag{37}$$

where m_i is the fictitious mass of node i , Δt the time step and ${K_i}^{max}$ corresponds to the highest stiffness value of the spring elements connected with the node i.

2.3.2. About segments of vanishing length

As previously described, in the deformed geometry the external forces are directed toward the bisectors of the angles formed by two successive tangents. It is then easy to prove from this equilibrium condition that if two successive concentrated forces have the same direction, in the deformed geometry, their two points of application coincide (see Figure 6). Yet, as it will be proved further (see expression (51)), the critical fictitious mass of nodes depends, for a sliding cable element, on the inverse of the minimal length between two consecutive points. To avoid numerical instability due to the vanishing of a segment, a series of springs, which depend on the length of each segment, are introduced. The stiffness of those springs is chosen in the form of a barrier function equal to zero when the length is above 5% of the initial segment length, and then equal to a logarithmic function of the length for lower values of the actual length. This numerical artefact helps convergence, avoids the collapse of any segment and visually does not affect the equilibrium shape (which can not distinguish between a 100% sliding and a 95% sliding).

2.3.3. Development of the stability condition

Hence, the stiffness matrix $\underline{\underline{K}}$ is defined as the summation of two real symmetrical matrices. $\underline{\underline{K}}$ is thus diagonalisable and all its eigenvalues are real. In order to establish a simple

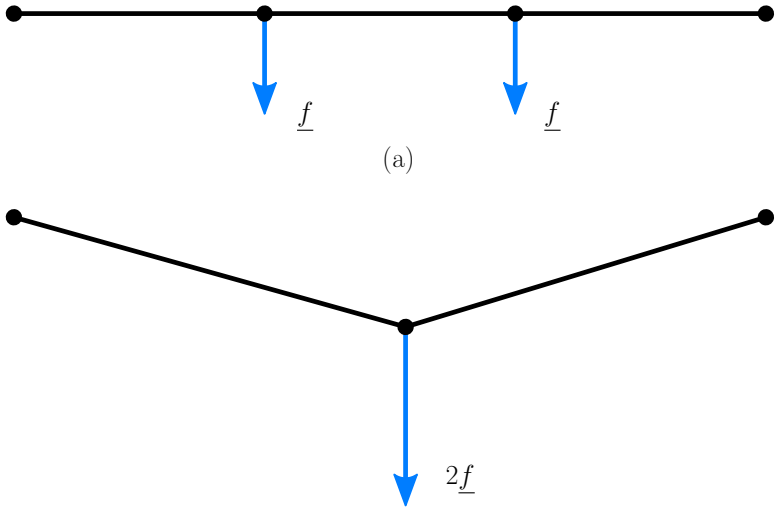

Figure 6: Limit of the frictionless sliding model under parallel forces.

analytic expression of ${K_i}^{max}$, the spectral radius of $\underline{\underline{K}}_E$ and $\underline{\underline{K}}_G$, $\rho\left(\underline{\underline{K}}_E\right)$ and $\rho\left(\underline{\underline{K}}_G\right)$ respectively, are separately determined. Indeed, in the particular case of a real and symmetrical matrix, the spectral radius is equal to the matrix 2-norm, so that the triangle inequality leads to:

$$\rho\left(\underline{\underline{K}}\right) = \rho\left(\underline{\underline{K}}_E + \underline{\underline{K}}_G\right) \leq \rho\left(\underline{\underline{K}}_E\right) + \rho\left(\underline{\underline{K}}_G\right) \tag{38}$$

To evaluate these two spectral radii we first establish that $\underline{\underline{K}}_E$ is a positive definite matrix. Let $\underline{X}$ be a non-zero vector of size $(3N)$. We may write:

$$\underline{X}^T \cdot \left[\underline{N} \otimes \underline{N}^T\right] \cdot \underline{X} = \left[\underline{X}^T \cdot \underline{N}\right]\left[\underline{N}^T \cdot \underline{X}\right] = <\underline{N}, \underline{X}>^2 \tag{39}$$

$\underline{N}$ being a strictly positive vector, $\underline{\underline{K}}_E$ is real and positive definite. Because all its eigenvalues are positive we have the obvious following upper bound:

$$\rho\left(\underline{\underline{K}}_E\right) < \mathrm{tr}\left(\underline{\underline{K}}_E\right) \tag{40}$$

From the analytic expression of $\underline{N}^T$ (13), we obtain:

$$\mathrm{tr}(\underline{N}\otimes\underline{N}^T) = 2+\sum_{i=2}^{n-1}\left[\left(\frac{\Delta x_{1,i}}{l_i}-\frac{\Delta x_{1,i-1}}{l_{i-1}}\right)^2+\left(\frac{\Delta x_{2,i}}{l_i}-\frac{\Delta x_{2,i-1}}{l_{i-1}}\right)^2+\left(\frac{\Delta x_{3,i}}{l_i}-\frac{\Delta x_{3,i-1}}{l_{i-1}}\right)^2\right] \tag{41}$$

By developing the sum:

$$\mathrm{tr}(\underline{N}\otimes\underline{N}^T) = 2+2\sum_{i=2}^{n-1}\left(1-\frac{\Delta x_{1,i-1}}{l_{i-1}}\frac{\Delta x_{1,i}}{l_i}+\frac{\Delta x_{2,i-1}}{l_{i-1}}\frac{\Delta x_{2,i}}{l_i}+\frac{\Delta x_{3,i-1}}{l_{i-1}}\frac{\Delta x_{3,i}}{l_i}\right) \tag{42}$$

Considering the series (θ_i) of angles between two consecutive vectors along the cable (see Figure 7), we may write the previous expression as follows:

$$\mathrm{tr}(\underline{N}\otimes\underline{N}^T) = 2\left[n-1-\sum_{i=2}^{n-1}\cos(\theta_i)\right] = 2\left[n-1-\sum_{i=2}^{n-1}\left(1-2\sin^2\left(\frac{\theta_i}{2}\right)\right)\right] \tag{43}$$

Because the sinus values range from -1 to 1:

$$\mathrm{tr}(\underline{N}\otimes\underline{N}^T) \leq 2\left[1+2\sum_{i=2}^{n-1}\left|\sin\left(\frac{\theta_i}{2}\right)\right|\right] \tag{44}$$

The expression (44) corresponds to the general case, where the nodes of the cable have three degrees of freedom in translation. And as it is, it can be implemented in the algorithm. In order to reduce the computational time, it is also possible to make simplifying assumptions and therefore to establish a simpler expression. In practice, the sliding cable is almost planar and its rotation angle θ is almost continuously increasing.. The value of its total curvature is thus lower than π (see Figure 7). Considering these assumptions, we know that all values of θ_i are in the range of 0 to π and hence all values of $\sin(\theta_i)$ are positive. Moreover, a current upper bound for the sinus is its argument. Therefore the expression (44) becomes in this particular case:

$$\mathrm{tr}(\underline{N}\otimes\underline{N}^T) \leq 2\left[1+\sum_{i=2}^{n-1}\theta_i\right] \tag{45}$$

Then by using the regularity of the cable's curvature, we establish a simple upper bound of the spectral radius of the $\underline{\underline{K}}_E$ matrix:

$$\rho\left(\underline{\underline{K}}_E\right) \leq 2K_0 \frac{l}{l_0}(1+\pi) \tag{46}$$

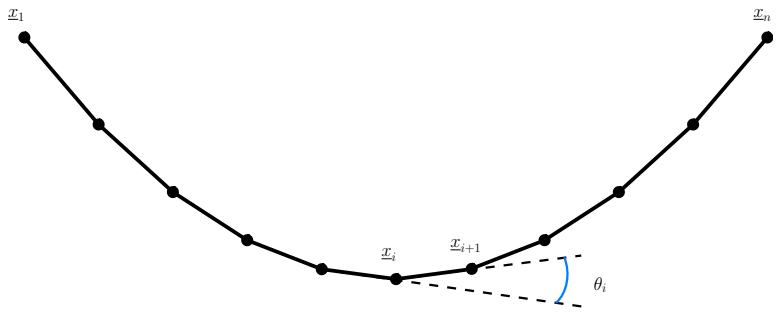

Figure 7: Sliding cable with continuously increasing rotation angle θ.

Now it remains to determine an upper bound for the spectral radius of $\underline{\underline{K}}_G$ defined in (36). To do this, we may use the Greshgorin circle theorem, which allows to calculate an upper bound of each eigenvalue of a diagonalisable matrix from its coefficients:

$$\rho\left(\underline{\underline{K}}_G\right) \leq K_0 \epsilon l_0 \max_{i\in[1;N-1]} \left\{ \sum_{j=1}^{n} \left| \underline{\underline{A}}_j \right| \right\} \tag{47}$$

which can be developed using (36):

$$\rho\left(\underline{\underline{K}}_G\right) \leq K_0 \epsilon l_0 \max_i \left\{ \sum_{k=1}^{3} \left(2\left|A_{i,(jk)}\right| + 2\left|A_{i-1,(jk)}\right| \right) \right\} \tag{48}$$

Then, using the expression (35) of the $\underline{\underline{A}}_i$ matrix, we get:

$$\rho\left(\underline{\underline{K}}_G\right) \leq K_0 \epsilon l_0 \max_i \left\{ 2\left(\frac{2}{l_i} + \frac{2}{l_{i-1}} \right) \right\} \tag{49}$$

By introducing l_{min} the length of the smallest segment, the following obvious upper bound can be established:

$$\rho\left(\underline{\underline{K}}_G\right) \leq 8K_0\epsilon\frac{l_0}{l_{min}} \tag{50}$$

Finally by grouping the upper bounds of the two spectral radii, we find the following inequality:

$$K_{max} \leq 2K_0\left[4\epsilon\frac{l_0}{l_{min}} + (1+\pi)\frac{l}{l_0}\right] \tag{51}$$

According to (37), the optimal nodal masses of a sliding cable in the dynamic relaxation scheme are thus defined by:

$$m_{opt} \geq \Delta t^2 K_0\left[4\epsilon\frac{l_0}{l_{min}} + (1+\pi)\frac{l}{l_0}\right] \tag{52}$$

Note that, conversely, the optimal time step of a sliding cable with n equal sliding masses in a centred explicit dynamic scheme would be defined by:

$$\frac{1}{\Delta t_{opt}} \geq \sqrt{\frac{K_0}{m_i}\left[4\epsilon\frac{l_0}{l_{min}} + (1+\pi)\frac{l}{l_0}\right]} \tag{53}$$

3. The ring cable model

A second application of the sliding cable model is proposed in this section. The ASM4 ring net is indeed composed of interlaced rings whose behaviour can be reproduced with a discrete model of a looped sliding cable (the square drawn in red in Figure 8). The discrete model used here is inspired from those of A. Volkwein and D. Coulibaly [28, 11] in which the ring is composed by the four contact points with the neighbour nodes.

The behaviour of one of these rings undergoing a two points tensile test is presented in Figure 8 taken from [22]. During the first stage its perimeter remains the same and only

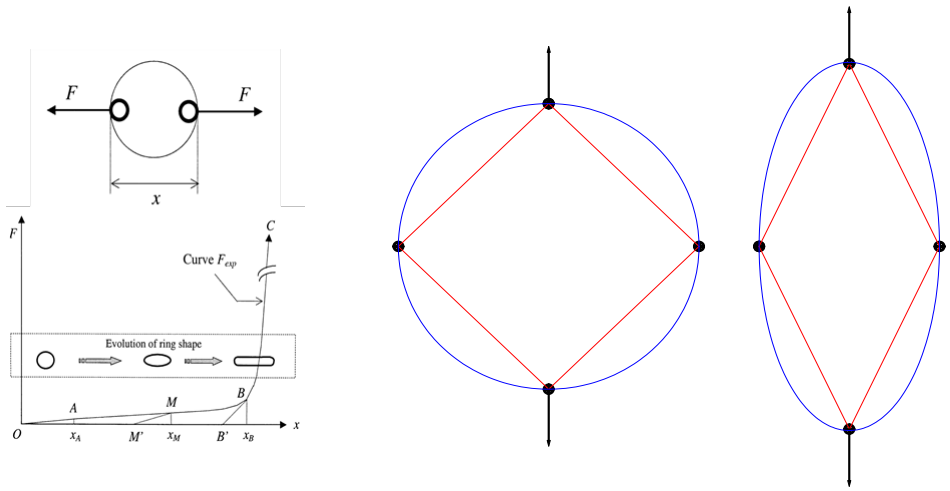

Figure 8: Experimental tensile test [22] and discrete ring model.

bending occurs. In the second stage, the length of the ring changes and axial stiffness of the rope is activated. The bending of the ring can be reproduced thanks to diagonal struts as in [28] but the strut stiffness is difficult to evaluate. Therefore we prefer here to integrate directly the bending stiffness in the tensile stiffness of the ring which will hence become nonlinear as in [11]. This kind of element will be called "ring element" in the rest of this paper and its characteristics will be identified in section 5.3.2.

The calculations allowing the determination of the ring cable tangent stiffness matrix are practically the same as those carried out in the case of the sliding cable. The only difference with (13) is the expression of the normal vector $\underline{N}$ for the first and last node which becomes:

$$\underline{N}^T = [t_{1,n} - t_{1,1}, \ldots, t_{1,i-1} - t_{1,i}, t_{2,i-1} - t_{2,i}, t_{3,i-1} - t_{3,i}, \ldots, t_{3,n-1} - t_{3,n}] \tag{54}$$

with:

$$\underline{t}_n = \frac{\underline{x}_1 - \underline{x}_n}{||\underline{x}_1 - \underline{x}_n||} \tag{55}$$

Taking into account this modification, the new expression of the $\frac{\partial \underline{N}_t}{\partial \underline{U}}$ matrix becomes:

$$\frac{\partial \underline{N}_t}{\partial \underline{U}} = \begin{pmatrix} \underline{\underline{A}}_n + \underline{\underline{A}}_1 & -\underline{\underline{A}}_1 & 0 & & & \cdots & 0 \\ & \underline{\underline{A}}_1 + \underline{\underline{A}}_2 & -\underline{\underline{A}}_2 & 0 & & \cdots & 0 \\ & & \ddots & \ddots & \ddots & \cdots & \vdots \\ & & & \underline{\underline{A}}_{i-1} + \underline{\underline{A}}_i & -\underline{\underline{A}}_i \quad 0 & \cdots & 0 \\ & sym & & & \ddots \quad \ddots & \cdots & \vdots \\ & & & & & \underline{\underline{A}}_{n-2} + \underline{\underline{A}}_{n-1} & -\underline{\underline{A}}_{n-1} \\ & & & & & & \underline{\underline{A}}_{n-1} + \underline{\underline{A}}_n \end{pmatrix} \tag{56}$$

where the $\underline{\underline{A}}_i$ matrices are defined as previously in (35).

The upper bound of $\underline{\underline{K}}_G$ spectral radius is the same as previously. However, due to changes in the expression of $\underline{N}$, the calculation of the upper bound of $\rho(\underline{\underline{K}}_E)$ is a little different. By keeping the same notations, we may rewrite the trace of $\underline{N} \otimes \underline{N}^T$:

$$\mathrm{tr}(\underline{N} \otimes \underline{N}^T) = 2 \sum_{i=2}^{n-1} (1 - \cos\theta_i) \tag{57}$$

There is no obvious simplifying assumption in the case of a n-nodes ring (a looped sliding cable with n nodes). In particular, the ring curvature may not be monotonic and the ring's convexity isn't ensured. Hence, the stability condition of a ring element depends on the number of its nodes:

$$\mathrm{tr}(\underline{N} \otimes \underline{N}^T) \leq 8n \tag{58}$$

Therefore, as previously the spectral radius of the tangent stiffness matrix may be estimated

by the following expression:

$$K_{max} \leq 2K_0 \left[4\epsilon \frac{l_0}{l_{min}} + 4n \frac{l}{l_0} \right] \tag{59}$$

Then by injecting this expression of K_{max} in (37), we can determine the critical fictitious mass in the case of a 4-nodes ring cable:

$$m_{opt} \leq 4\Delta t^2 K_0 \left(\epsilon \frac{l_0}{l_{min}} + 4 \frac{l}{l_0} \right) \tag{60}$$

From these two relations on the spectral radius of the sliding cable and the ring cable, we are able to ensure the stability of these two elements implemented inside a dynamic relaxation code. The modelling and the computations of a whole barrier does not present other major difficulties. In the next section, we hence propose two simple case studies to verify the results given by the sliding cable model and to assess the accuracy and efficiency of the method. Then, a more elaborated example will be shown in the fifth section.

4. Two simple examples of structures using sliding cables

4.1. Equilibrium of a module sliding along a cable

4.1.1. Presentation of the structure and analytic model

The structure studied here was already used as elementary problem by A. Volkwein and L. Ghoussoub in their PhD [28, 17]. It is formed by a four points sliding cable and a module transporting a load. This module is fixed to the two middle points of the cable and represents the loading undergone by a net during a block impact. The whole structure is hold by the two extremities of the sliding cable as shown in Figure 9. The module is formed by two bars

of length h holding a beam of length d. The initial length of the sliding cable (which can be prestressed) is l_0.

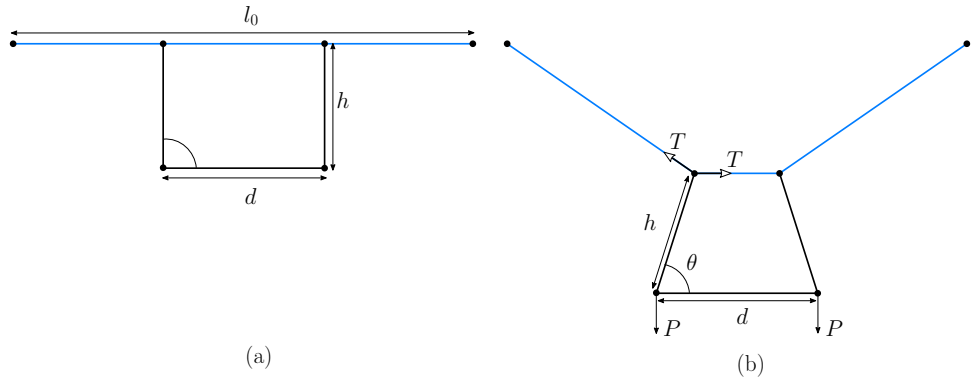

Figure 9: Analytic model before and after loading.

We assume that the members stiffness of the module are much higher than the one of the sliding cable, and thus the module's member can be considered non-deformable.

The equilibrium state of this structure can thus be analytically determined. The equilibrium of one of the sliding points is given by:

$$P = 2T\sin(\theta) \tag{61}$$

Moreover, the tensile load in the cable can be expressed according to its deformation and prestress by:

$$T = K\Delta l + T_0 \tag{62}$$

where K is the stiffness of the cable, Δl its elongation and T_0 the initial prestress. By writing the cable deformation according to the angle θ (cf. Figure 9):

$$l = f(\theta) \tag{63}$$

$$\Delta l = f(\theta) \tag{64}$$

and injecting this expression in equation (61), we find the relation between the weight of the module and the geometric deformation of the cable:

$$P = K \tan(2\theta) \left(1 + \cos(2\theta)\right) \left(d - 2h\cos(\theta) - l_0\right) + T_0 \sin(2\theta) \tag{65}$$

4.1.2. Comparison between analytic and numerical results

The structure presented in previous paragraph is modelled with its loading inside the dynamic relaxation tool. Simulations are carried out for different values of the load P to observe the evolution of the system. The initial length of the cable is $l_0 = 40m$ and its stiffness is $K = 1250N.m^{-1}$, the dimensions of the module are $h = 11m$ and $d = 14m$. In the first simulations series the sliding cable is not prestressed ($T_0 = 0$). Figure 10 shows the evolution of the P load according to the θ angle for the numerical and analytic results. We remark that for a non-prestressed cable the numerical results perfectly correspond to the analytic results, with an almost 0.3% error on the whole load path.

We then carry out the same simulations adding prestress to the cable with a tension of $T_0 = 2000N$. Once again, we observe that the numerical results are in good agreement with the analytic model, and this time, the average error is less than 0.1%. The stiffening effect of the prestress is well reproduced by the model. For this case study (with or without prestress) the computational tool reproduces successfully the geometrical non-linearities due to the large vertical deformation of the cable.

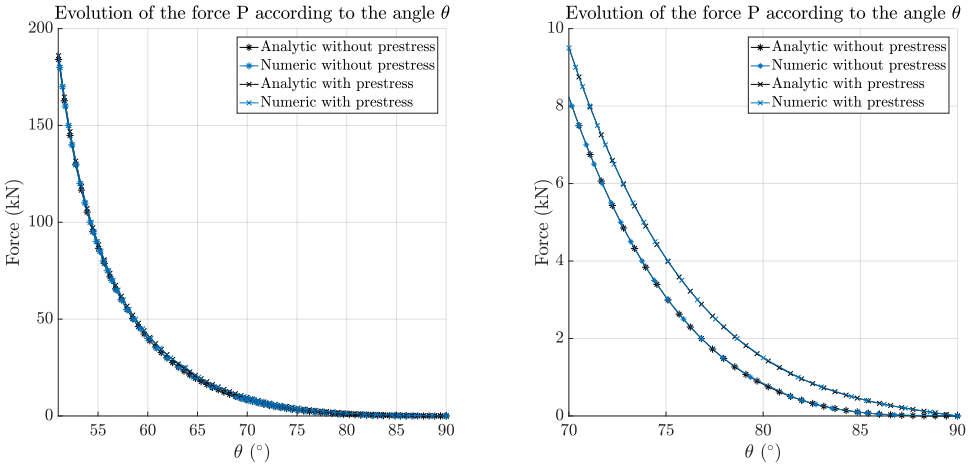

(a) (b)

Figure 10: First case study "simple cable": comparison between analytic and numerical results with and without prestress.

4.2. Study of a symmetric structure comprising multiple sliding cables

4.2.1. Definition of the model

The accuracy of the model is tested here for a problem where several sliding cables are connected while allowing relative sliding between them. The structure is presented in Figure 11. It is formed by two symmetrical pairs of sliding cables: the long ones, drawn in red, connect six points: $(P_1, A, B, C, B_{bis}, P_{2bis})$ for the left side and $(P_2, B, C, B_{bis}, A_{bis}, P_{1bis})$ for the right side, and the short ones, drawn in blue, connect each one three points (P_1, A, P_2) and $(P_{2bis}, A_{bis}, P_{1bis})$ for the left and the right sides respectively. In addition to these four cables there are two symmetrical bars (A, B) and (B_{bis}, A_{bis}), drawn in black.

The two cables pairs, which constitute the structure, have the same stiffness. The stiffness of the two bars is variable in the study: it actually controls the relative sliding between the cables. The equilibrium state of this system is solved on one hand with the dynamic relaxation tool and on the other hand with a non-linear solver implemented in the soft-

ware matlab® and using a trust-region algorithm (see J. Moré 1983 [21]). The problem is controlled in displacement by the vertical motion of the point C. The position of points $P_1, P_2, P_{2,bis}$ and $P_{2,bis}$ are fixed. The resolution of the problem by the trust-region algorithm consists simply in solving a four-dimensional non-linear system, given by the equilibrium equations of points A and B and in which the unknown parameters are the positions of these two points.

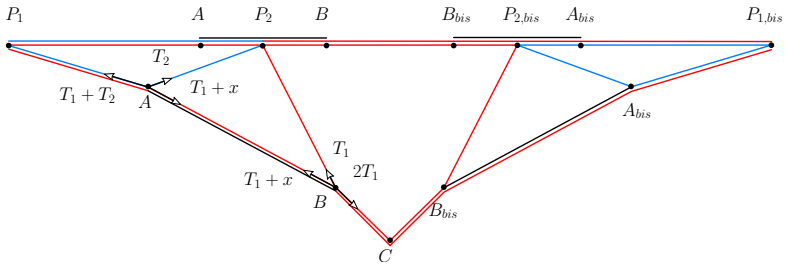

Figure 11: Second case study: Multiple sliding cables model.

The relaxed lengths are given by the initial geometry which is described below, by taking into account the symmetry of the problem:

$$P_1C = 7.5\,m\,, \quad P_2C = 2.5\,m\,, \quad AC = 4.25\,m\,, \quad BC = 1.75\,m \tag{66}$$

The four cables have the same bi-linear elastic behaviour with two stiffnesses respectively before and after the threshold: $k_{c1} = 106\,kN.m^{-1}$ and $k_{c2} = 3,6\,kN.m^{-1}$. They have also the same threshold: $\epsilon_{lim} = 2.3\%$, so that the lateral cables reach it for a twice lower tensile stress. These bi-linear behaviours mimic the side cables in rockfall barrier which are generally linked with dissipating energy devices conferring to the set "cable + brakes" this material

non-linearity. The bar's behaviour is elastic with a stiffness of: $k_b = 0,8\,kN.m^{-1}$ for the first two computation series whose results are presented in the figures 12 and 13. It illustrates the role of the cable net in the control of the sliding cable geometry.

4.2.2. Comparison of results

This simplified model of rockfall barriers presents some key aspects of their behaviour, especially the connection of two sliding cables via the net (here modeled by the bar AB). Graphs in Figure 12 present the comparison of computation results obtained with the trust-region and the DR algorithms. We can observe that the kinematics of the structure given by the four unknowns of this static problem (Graph (b) and (c) of Figure 12) are identical with an error smaller than 0.1%. For very small vertical displacement of the structure ($Y_c < 20$cm), we observe that motions of A and B are larger than during the rest of the loading path. It can also be noted that A moves away from the loaded zone during this first displacement, while it moves toward the loaded zone afterwards.

Another significant result concerns the whole behaviour of the structure (Graph (a) of Figure 12): the second phase of the behaviour, after passing the threshold of the central cable, is remarkably linear. Figure 13 highlights this impact of the yielding of the two central cables. The stiffness of the whole structure increases until the central cables reach their threshold. After the threshold and during this linear phase, the apparent stiffness remains constant. Thus we observe that, even if the tensile force in lateral cables is not negligible compared to the one in central cables (almost 50%), its influence on the whole behaviour remains limited as it changes little the structure's geometry.

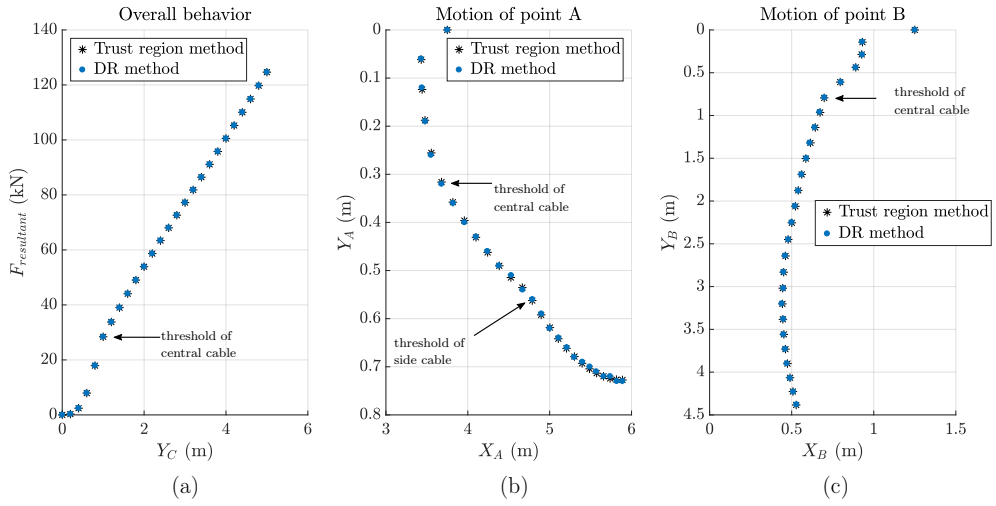

Figure 12: Comparison of the DR method with a non-linear algorithm implemented in matlab.

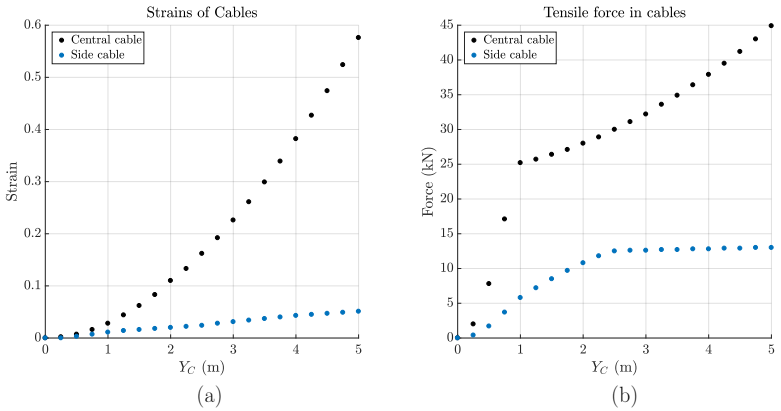

Figure 13: Cables load path for increasing displacements in the multiple sliding cables model.

4.2.3. Convergence of the DR algorithm

The purpose of this last paragraph is to present some issues about the convergence and the stability of the DR algorithm. The calculations of the fictitious masses are given by the expression (52) and the current safety coefficient $g = 1.05$ ([4, 14]). The parameters of the first simulations series are used. We consider the equilibrium of the structure for a given vertical displacement of the point C: $Y_C = 5\,m$. The calculations are carried out by applying to the structure a given displacement or a given force. In each loading case, the load is reached in two different ways: in a series of 25 "incremental steps" (the step length is $0.2m$ for the study in displacement and $5.0kN$ for the study in force) and in a single step. The results of these four series of simulations are presented in Table 1 and compared with the result given by the trust region method. We see that whatever the loading mode, the calculation converges toward the same solution with a high accuracy which highlights the relevance of dynamic relaxation when only one equilibrium positions is looked for.

	$F_{resultant}$ (kN)	Y_C (m)	X_A (m)	Y_A (m)	X_B (m)	Y_B (m)
trust region method	124.6	5.00	5.89	0.73	0.53	4.38
incremental displacement	124.6	5.00	5.89	0.73	0.53	4.38
one step displacement	124.6	5.00	5.89	0.73	0.53	4.38
incremental force	124.6	5.00	5.89	0.73	0.53	4.38
one step force	124.6	5.00	5.89	0.73	0.53	4.38

Table 1: Comparative convergence study with DRM.

4.2.4. Parametric study of the bar stiffness

In a second simulations series, we propose to study the impact of the parameter k_b (the stiffness of the bar) on the behaviour of the structure. The vertical positions of the point C is fixed at the altitude $Y_C = 5\,m$ and the stiffness parameter changes in the range $10^3\,N < k_b < 10^8\,N$. Once again the computations are carried out with the two algorithms. The results are presented in Figure 14. We see that the increase of the bar stiffness has significant influence on the equilibrium geometry but relatively little on the reaction force. Points A and B slide towards each other, so that the lengths of the two central sliding cables increase as the lengths of the bars decrease.

Note that, with the parameters (stiffness and geometry) chosen here, the range under $10\,kN$ is not accessible with the two algorithms. Indeed, the positions of points P_1, P_2 and C form a minimum sliding angle which is reached when the bar is completely elongated and points A and P_1 as well as B and P_2 coincide respectively (see Figure 15). Considering this minimum angle and the tensile force in the central cables, it is possible to define the minimum force the bar has to apply to the point B to balance it. To this end, we write the equilibrium of the point B located at the same place as the point C. Considering the notations of the Figure 15, where the force x applied by the bar to the point B and the angle α_3 are the two unknown parameters of the system:

$$\begin{cases} T_1\cos(\alpha_1) + (T_1 + x)\cos(\alpha_2) = 2T_1\cos(\alpha_3) \\ T_1\sin(\alpha_1) + (T_1 + x)\sin(\alpha_2) = 2T_1\sin(\alpha_3) \end{cases} \tag{67}$$

Considering this final geometry, we find that the equilibrium of the point B can be ensured by the force $x = 3,09\,kN$ and the angle $\alpha_3 = 42^\circ$. At this point, two remarks

should be made. First, this force is indicative and in practice the variations of the bar stiffness change the equilibrium geometry presented in Figure 15. Second the geometry of Figure 15 is the exact solution of the problem corresponding to the limit case (for which the stiffness of the bar is null). Due to the nature of the sliding cable which ensures the same tension between each couple of nodes and because in practice two points can not perfectly coincide, this limit case can not be reached numerically.

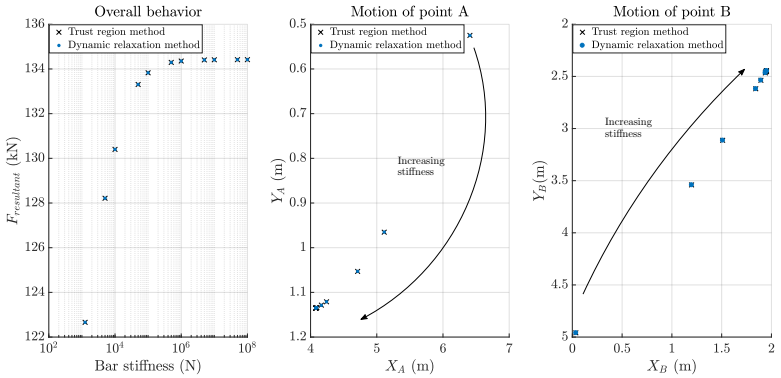

Figure 14: Influence of the bar stiffness on the behaviour of the structure.

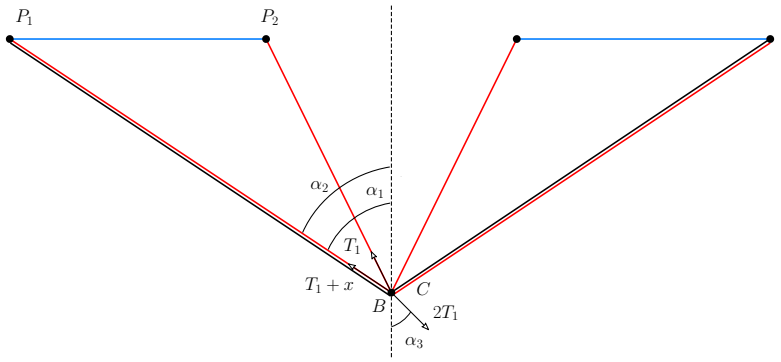

Figure 15: Limit equilibrium with a very low stiffness of the bar.

4.3. Conclusion

Through these two comparative studies, we have tested on simple cases the accuracy and the stability of our numerical models of sliding cables. For both comparisons with analytic models (4.1) or with computations carried out with another algorithm (4.2), the results of the numerical simulations are in perfect agreements. This allows us to confidently model a complete barrier.

5. A case study: numerical simulation of a full-scale experiment

5.1. Structure description and presentation of the experimental conditions

In this section, we present the numerical simulation of one of the experiments carried out in the framework of the French national project C2ROP (www.c2rop.fr) which brings together many public and private partners around the topics of landslide risk and protection devices. The numerical tool, initially developed in the laboratoire Navier for elastic gridshells [14], works within the framework of Rhinoceros 3D and its plugin Grasshopper.

5.1.1. Barrier architecture

The scheme of the tested barrier is presented in Figure 16 and has been detailed in [10]. A three-modules barrier is anchored perpendicularly to a vertical cliff. The whole fence is $2.75m$ high and $15m$ long ($5m$ for each modulus). This fence consists of 10 support cables (4 on each edge parallel to the cliff and 1 on each lateral edge). With this layout, the sliding of the net is possible along each edge. Because of the large span of such structures, the wiring along the edge is generally complex. It is presented in Figure 17. It is symmetric

between the upstream and downstream edges. The two lateral cables (in green in Figure 17) hold the small edges of the net. The two external cables link the lateral anchor with the head of the central post (cables A and A_{bis} in blue) and two central cables connect the head of the first and third posts (cable B and B_{bis} in red). Each cable holds partially the net and is free near the post's head to avoid stress concentration. With this assembly, the net is hold by two cables in the centre of the modulus and by a single cable near posts. The set formed by the net and the support cables is hold to the cliff by 4 steel posts (modelled by beam elements). Finally, the head of each post is maintained by 3 cables (two upstream and one downstream), anchored to the cliff (see Figure 16). Brake elements (so called snake brakes in which a cable winds rubbing along a set of screws) are connected in series with each support cable.

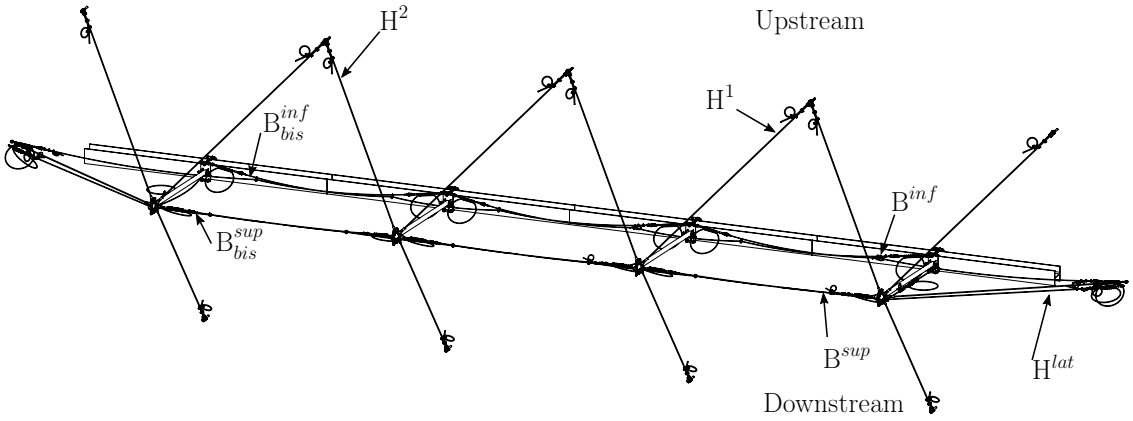

Figure 16: Technical drawing of the tested barrier (Courtesy of PN C2ROP).

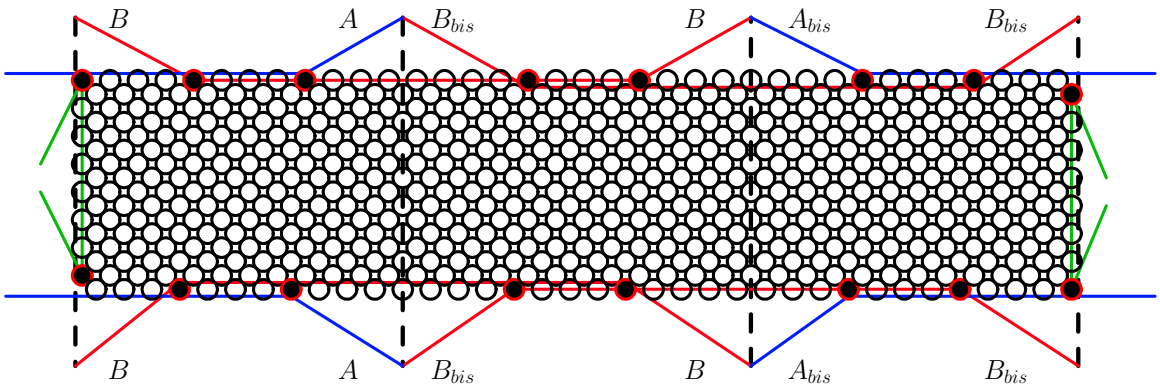

Figure 17: Support cables nomenclature and weaving principle scheme.

5.1.2. Loading

The position of every post foot is fixed but the rotation of the post is free. The positions of all cable anchors on the cliff are also fixed. The links between cables and posts or cables and brakes are hinges. The sliding of the net on the surrounding cables is free.

A quasi-static loading is then applied to the structure. A $740kg$ normalised polyhedral-shaped concrete block is maintained by a winch and slowly placed in the middle of the net until the barrier reaches equilibrium under dead-weight and block load. Then, another winch is hooked on the bottom part of the block and pulled orthogonal to the net (see Figure 18). Its vertical displacement is controlled and step by step increased so that the loading can be considered as quasi-static. Several load cells are put on the fence components enabling the stresses in all the support cables and in some anchoring ropes to be recorded (see black flags in Figure 17). The resultant load applied to the winch is also recorded.

Figure 18: Front view of the quasi-static experiment on the rockfall barrier prototype (Courtesy of PN C2ROP).

5.2. Superstructure and loading modellings

The experimental loading being monotonic, the behaviour of all the elements is considered reversible (elastic but not necessarily linear). The relaxed length of each barrier component is given by the initial geometry of the structure (no prestress is taken into account). The stiffness are identified from preliminary experiments on the components (brake, cable and net) separately. The behaviour of the ring net is studied in detail in section 5.3.2. Sliding cables and brakes being set in series in the experiment, they are merged in the numerical model into a unique bi-linear sliding cable element for simplicity reasons. The first stiffness corresponds to the stiff behaviour of the brake (before its scrolling), the second stiffness is low in comparison and corresponds to the brake's scrolling. The behaviour of anchoring cables is simply modelled thanks to a linear law giving the stress according to the relative displacement of the two cable endpoints. The steel posts are modelled as truss elements with a similar linear law.

The block shape used for the numerical simulations is not polyhedral but spherical. Its diameter is $0.85m$ and corresponds to the sphere tangent to the edges of the polyhedron. Contact is modelled with many bar elements, which work only in compression and whose relaxed lengths correspond to the block radius. The tensile stiffness is null and the behaviour is linear elastic in compression. The stiffness is determined according to the maximum tensile force applied to the structure and the tolerance of the interpenetration level. With a maximum force of almost $210kN$ and a tolerance of $1cm$, the stiffness of the block bar is set to: $K_{block} = 5.10^6$kN/m. As in the experiment, the simulations are carried out by imposing the block displacement (the convergence is quicker than by imposing a force on the block).

5.3. Numerical modelling of the ring net

5.3.1. Experimental setup

Unlike the case studies carried out previously on the sliding cable, the ring cable model is calibrated thanks to a comparison with a plane tensile experiment. This experiment was also carried out in the framework of the french national project C2ROP. The experimental setup consists of a square ring net (three by three) which is pulled in one direction and maintained in the perpendicular one (cf. Figure 19). The test is driven in displacement and load cells measure reaction forces in the two directions. The results are given according to the axial displacement of the moving edge (see Figure 20).

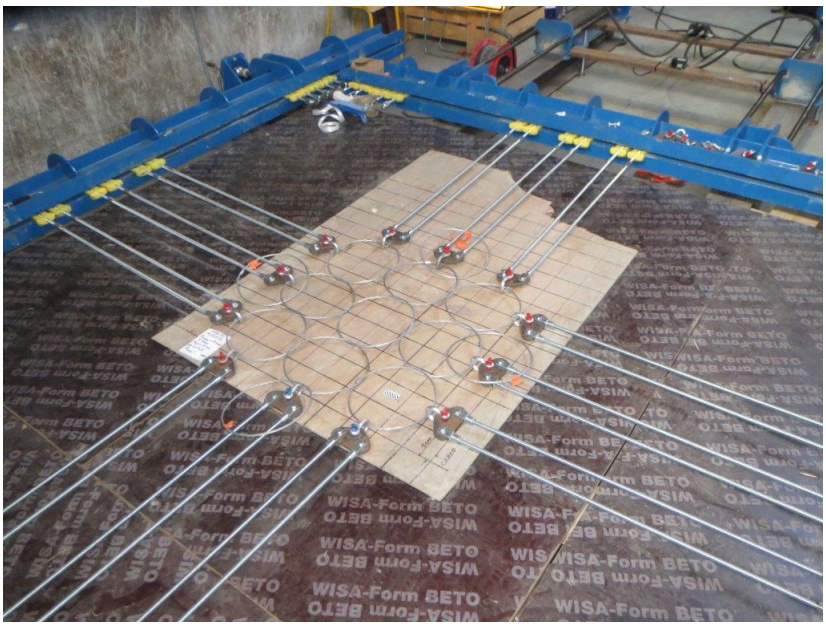

Figure 19: Experimental setup of the plane tensile test on a ASM4 ring net (Courtesy of PN C2ROP).

5.3.2. Numerical simulation and description of the ring model

The basic pattern of a single ring is described in Figure 8. By assuming that the ring deformation is uniform in the square net, the tensile behaviour of a single ring can be identified from the experimental results in the loading direction. Indeed, by referring to Figure 20, the equilibrium of the point A gives the tensile force in the ring, while its strain is calculated from the axial displacement. The constitutive law is then continuously identified, thanks to the least squares method, by a five order polynomial:

$$K_0(\epsilon) = 3.56.10^9\epsilon^5 - 6.80.10^8\epsilon^4 + 3.95.10^7\epsilon^3 - 4.07.10^5\epsilon^2 + 3.55.10^3\epsilon \tag{68}$$

where ϵ is the strain of the ring, which is defined according to d_{ring}, the initial diameter of a ring, and ΔL, the overall axial elongation.

$$\epsilon = \frac{\sqrt{d_{ring}^2 + (d_{ring} + \frac{\Delta L}{3})^2} - \sqrt{2}d_{ring}}{\sqrt{2}d_{ring}} \tag{69}$$

We note that a 5 degree polynomial is enough to correctly reproduce the curve behaviour. However this polynomial fits the experimental behaviour only for the strains reached during the test. The behaviour modelled numerically is extended by the tangent at the maximum strain really allowed for larger strains (the rupture of the elements is not taken into account in the numerical computations). We remark then that the behaviour fit on the axial load is also in accordance with the experimental results in the transverse direction. Indeed, for small axial displacements, it is obvious that the Poisson's ratio is close to one for both continuous real ring and discrete model (see Figure 20). Moreover, since for large displacements, the deformed geometry of the real ring and discrete model are the same, the Poisson's ratio

observed in the simulations is always in agreement with the experiment. The material stiffness of the ring is linearly linked to its dimensions so that the expression (68) of the constitutive law does not depend on the net density, which is practically the same as the one of the real net.

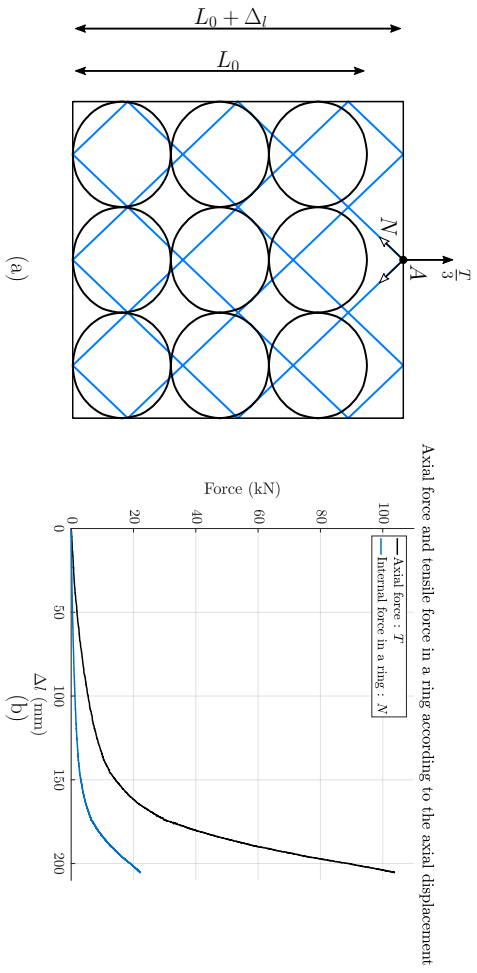

Figure 20: Experimental results of the plane tensile test.

All information relative to the elements stiffness can now be regrouped in Table (2).

Component	behaviour	Characteristics		
sliding cable + brake (upstream/downstream)	bi-linear in traction	before threshold $ES = 1140kN$	threshold level $25kN$	after threshold $ES = 35kN$
sliding cable + brake (lateral cables)	bi-linear in traction	before threshold $ES = 1190kN$	threshold level $25kN$	after threshold $ES = 35kN$
12 anchoring cables	traction only	$ES = 1260kN$		
rings	polynomial	5^{th} degree, fit on the plane tensile test (68)		
bars of the block	compression only	$ES = 10^7kN$		

Table 2: Synthese of all barrier components stiffness.

5.4. Comparison with the numerical simulation

This section compares the experimental results and the numerical simulations for the overall response of the barrier (the resultant force applied to the winch) and also for the tensile load in two barrier components (support cables). In all this section we will refer to the drawing (17) which gives a nomenclature of the barrier components.

5.4.1. Overall barrier behaviour

Rather than comparing the resultant force applied to the block centre to the experimental force applied to the winch, we prefer here to consider the global stored elastic energy. Experimental results are thus integrated to the vertical displacement of the winch (see Figure 21). We observe that the numerical simulations are in good agreement with the experiment. For

both, experimental and numerical results, the resultant force applied to the winch increases almost linearly according to the block's vertical displacement. This result is surprising. Indeed the large displacements in the structure and the sliding of the net along the support cables involves necessarily geometrical non-linearities. Moreover, the mechanical behaviour of the support cables is also non-linear. The complex overall behaviour of this structure, which is nevertheless well reproduced by the numerical model, requires more data to be more accurately described including the evolution of the local stress according to the actual geometry of the barrier. Detailed investigation of the behaviour is foreseen in a next paper.

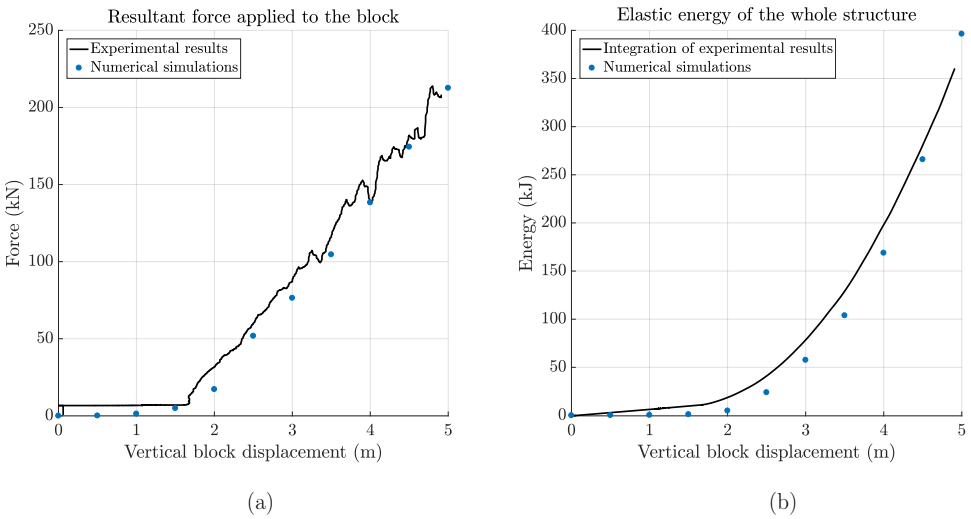

Figure 21: Experiment test vs. numerical simulation.

5.4.2. Tensile stress in the central support cables

The tensile stress is recorded for the two (upstream and downstream) central cables called B in Figure 17 and located on the left side of the barrier. Because the experimental model is not completely symmetric there is a significant difference between the tensile stress

in the cables B and B_{bis} (probably because of some asymmetry in the prestress level). For this reason, we prefer to compare an average of the tensile stresses in the two upstream and downstream cables (see Figure 22). Further on, names of cables will refer to the Figure 18.

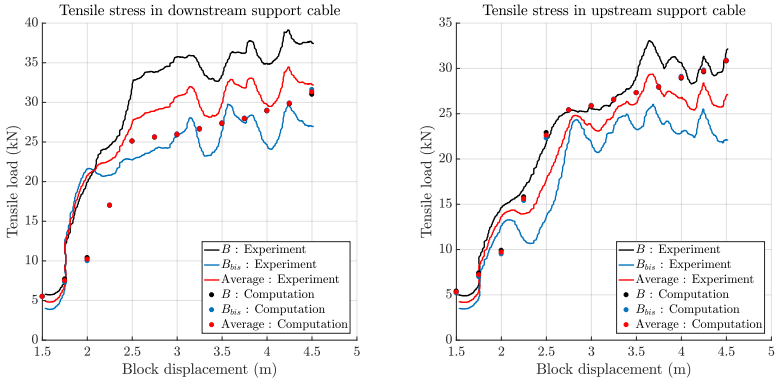

(a) (b)

Figure 22: Central support cables behaviour: experiment test vs. numerical simulation. (a) : Resultant force applied to the block, (b) : Elastic strain energy of the whole structure.

We can observe that, for the two edges, the measures on the cables B and B_{bis} give relatively remote results, particularly for the second stage of the behaviour during which the brakes scroll. The slight asymmetry of the structure has a limited impact on numerical results. We can also note that the effective threshold levels are different from the expected value of $25kN$, in particular for the downstream support cables. This is probably due to existing prestress in the experimental structure prestress which is not taken into the simulation but which is implemented in the model and could in principle be introduced into the simulation). The comparison between the experiment and the simulations is hence carried out from the averaged results. For the downstream cables, the threshold of the brakes elements seems to happen for the same displacement of the block and the behaviours after it are similar. However, the first stiffness are different between both curves: in the

experiment, during a first stage the net is the only barrier component which is activated and the forces are then faster transferred to the support cable, whereas this transfer is gradual in the numerical simulations. Regarding now the tensile load in the upstream support cables, we observe that, this time, the results are close, even if the stiffness before and after the thresholds of the brakes are slightly different.

The numerical results presented here are thus in good agreement with the experimental results. The dynamic relaxation method associated with frictionless cable reproduces well the behaviour of the whole structure and gives good results for the components considered separately. This validates a posteriori the hypothesis that, for the type of structures tested here, the friction does not have a significant influence on the equilibrium configuration and in the forces in the supporting members. It can thus be considered as a valuable alternative to find very quickly equilibrium shapes of rockfall barriers in an early design phase and to test the behaviour of a large variety of alternative designs.

Furthermore, we recall here that this result is also a consequence of the existence of brakes attached at the end of the sliding cables that cut off dynamic peaks in the supporting structure. As said in the introduction, the net is not protected by the brakes and thus see the dynamic effects of the loading. Therefore, in early phase design, we advise that the engineer complete the quasi-static simulations by a verification of the bullet effect following for example [19]. Then, for detailed design of the barrier, only full dynamic simulations with friction along the sliding cables will give the required accuracy for a reasonnably optimised sizing of the structural members. At this late design phase, there sould no more be any need for testing of alternative structures and the computational cost of the complete dynamic

simulations should not be a problem.

6. Conclusion

In this paper we proposed a continuous model for frictionless sliding cables and its discretization. It was used for a simple estimation of the sliding cable mass parameters ensuring the stability of the finite difference scheme in the framework of the dynamic relaxation method. This estimation was determined by evaluating an upper bound of the spectral radius of the tangent stiffness matrix for two specific cases: the n-nodes sliding cable and the ring cable which is formed by closing a sliding cable. The numerical performance of these two elements have been tested and the numerical simulation of a quasi-static loading test on a complete barrier prototype was shown. Although quasi-static experiments on whole structure are rare in the literature, they are a necessary step to carry out dynamic simulations, because they allow to verify the assembly of the barrier components model, which are frequently calibrated by means of quasi-static tests. Hence in these case-studies, the simulations have shown very good agreement with reference problems.

In further work, dynamic simulations will be carried out by extending the proposed stability conditions to estimate the maximum time step ensuring the numerical stability. The extension is straight forward if lumped mass matrices are assumed, but requires some developments in the general case. The final aim of the study would be to conduct a comparative study between the quasi-static and the dynamic calculations to further investigate the similarities and differences of the two approaches and to produce equivalent acceleration models for the design of these structures.

Acknowledgements

The experiments presented in this paper were carried out in the framework of the French national project C2ROP. The authors wish to thank all the members of the national project and particularly the members of the working group on soft barriers for their invaluable support, namely M-A. Chanut and J. Coulibaly from CEREMA, P. Robit, I. Olmedo from GTS, C. Galandrin from CAN and D. Bertrand from INSA Lyon.

References

[1] A. Albaba, S. Lambert, F. Kneib, B. Chareyre, and F. Nicot. DEM Modeling og a Flexible Barrier Impacted by a Dry Granular Flow. *Rock Mechanics and Rock Engineering*, 50:3029–3048, 2017.

[2] M. Aufaure. A finite element of cable passing through a pulley. *Computers and Structures*, 46(5):807–812, 1993.

[3] M. Aufaure. Three-node cable element ensuring the continuity of the horizontal tension; A clamp-cable element. *Computers and Structures*, 74(2):243–251, 2000.

[4] M. R. Barnes. Form Finding and Analysis of Tension Structures by Dynamic Relaxation. *International Journal of Space Structures*, 14(2):89–104, 1999.

[5] N. Bel Hadj Ali, L. Rhode-Barbarigos, and I. F. Smith. Analysis of clustered tensegrity structures using a modified dynamic relaxation algorithm. *International Journal of Solids and Structures*, 48(5):637–647, 2011.

[6] N. Bel Hadj Ali, A. C. Sychterz, and I. F. Smith. A dynamic-relaxation formulation for analysis of cable structures with sliding-induced friction. *International Journal of Solids and Structures*, 126-127:240–251, 2017.

[7] D. Bertrand, A. Trad, A. Limam, and C. Silvani. Full-scale dynamic analysis of an innovative rockfall fence under impact using the discrete element method: From the local scale to the structure scale. *Rock Mechanics and Rock Engineering*, 45(5):885–900, 2012.

[8] M.-A. Chanut, L. Dubois, and F. Nicot. Dynamic behavior of rock fall protection net fences: a parametric study. *Engineering Geology for Society and Territory*, 2(January):1863–1867, 2015.

[9] Z. H. Chen, Y. J. Wu, Y. Yin, and C. Shan. Formulation and application of multi-node sliding cable element for the analysis of Suspen-Dome structures. *Finite Elements in Analysis and Design*, 46(9):743–750, 2010.

[10] J. Coulibaly, M.-A. Chanut, S. Lambert, and F. Nicot. Sliding cable modeling: An attempt at a unified formulation. *International Journal of Solids and Structures*, 130-131:1–10, 2018.

[11] J. B. Coulibaly, M.-A. Chanut, S. Lambert, and F. Nicot. Nonlinear Discrete Mechanical Model of Steel Rings. *Journal of Engineering Mechanics*, 143(9):04017087, 2017.

[12] P. Cundall. A computer model for simulating progressive large scale movements in block rock systems. In *Symposium International of the Society of Rock Mechanics*, 1971.

[13] A. Day. An Introduction to Dynamic Relaxation. *the engineer*, pages 218–221, 1965.

[14] C. Douthe and O. Baverel. Design of nexorades or reciprocal frame systems with the dynamic relaxation method. *Computers and Structures*, 87(21-22):1296–1307, 2009.

[15] EOTA. Etag 027. Technical Report April 2013, European Organisation for Technical Approvals, 2013.

[16] C. Gentilini, L. Govoni, S. de Miranda, G. Gottardi, and F. Ubertini. Three-dimensional numerical modelling of falling rock protection barriers. *Computers and Geotechnics*, 44:58–72, 2012.

[17] L. Ghoussoub. *Analyse de quelques éléments du comportement des écrans de filets pare-blocs*. PhD thesis, Université Paris Est, 2015.

[18] H. Grassl, A. Volkwein, E. Anderheggen, and W. J. Ammann. Steel-net rockfall protection: Experimental and numerical simulation. *Structures under Shock and Impact VII*, pages 143–153, 2002.

[19] J. P. Hambleton, O. Buzzi, A. Giacomini, M. Spadari, and S. W. Sloan. Perforation of flexible rockfall barriers by normal block impact. *Rock Mechanics and Rock Engineering*, 46(3):515–526, 2013.

[20] K. Hincz. Nonlinear Analysis of Cable Net Structures Suspended From Arches with Block and Tackle Suspension System, Taking into Account the Friction of the Pulleys. *International Journal of Space Structures*, 24(3):143–152, 2009.

[21] J. More and D. Sorensen. COMPUTING A TRUSTREGION STEP. *Society for Industrial and Applied Mathematics*, 4(3):553–572, 1983.

[22] F. Nicot. *Etude du comportement mécanique des ouvrages souples fr protection contre les éboulements rocheux*. PhD thesis, Centrale Lyon, 1999.

[23] I. Olmedo, R. P., BertrandD., G. C., C. J. B.., and C. M-A. Extended experimental studies on rockfall flexible fences. In *Proceedings of Rocexs 2017 Barcelona Spain*, 2017.

[24] M. Papadrakakis. A method for the automatic evaluation of the dynamic relaxation parameters. *Computer Methods in Applied Mechanics and Engineering*, pages 35–48, 1981.

[25] D. Peila, S. Pelizza, and F. Sassudelli. Evaluation of Behaviour of Rockfall Restraining Nets by Full Scale Tests. *Rock Mechanics and Rock Engineering*, 31:1–24, 1998.

[26] P. V. Tran, K. Maegawa, and S. Fukada. Prototype of a wire-rope rockfall protective fence developed with three-dimensional numerical modeling. *Computers and Geotechnics*, 54:84–93, 2013.

[27] D. Veenendaal and P. Block. An overview and comparison of structural form finding methods for general networks. *International Journal of Solids and Structures*, 49(26):3741–3753, 2012.

[28] A. Volkwein. *Numerische Simulation von flexiblen Steinschlagschutzsystemen*. PhD thesis, ETH, 2004.

[29] B. Zhou, M. L. Accorsi, and J. W. Leonard. Finite element formulation for modeling sliding cable elements. *Computers and Structures*, 82(2-3):271–280, 2004.